



# Direct observations of negative ions on the Lunar surface by Chang'E-6



Martin Wieser<sup>1,5</sup>✉, Aibing Zhang<sup>2,3,5</sup>✉, Romain Canu-Blot<sup>1,5</sup>, Wengjing Wang<sup>2,3,5</sup>, Gabriella Stenberg Wieser<sup>1</sup>, Lianghai Xie<sup>2</sup>, Stas Barabash<sup>1,5</sup>, Tianhua Zhong<sup>2,3</sup>, Xiao-Dong Wang<sup>1</sup>, Yongliao Zou<sup>2</sup>, Máté Kerényi<sup>1</sup>, Weibin Wen<sup>4</sup>, Charles Lue<sup>1</sup> & Chi Wang<sup>2,3</sup>

The solar wind can interact directly with the surface of airless bodies like the Moon. The interaction causes sputtering of surface materials and solar wind ions are also partially backscattered to space. Particles leaving the surface can have any charge-state. At the Moon, backscattered or sputtered positive ions<sup>1–4</sup> and energetic neutral atoms<sup>5–8</sup> have been observed, but all attempts to find negative ions in electron measurements have failed so far. Here we present measurements by Chang'E-6 from the lunar farside<sup>9</sup> revealing the existence of a layer of negative ions close to the lunar surface. We found that about  $2.5^{+1.2}_{-0.8}\%$  of the impinging solar wind protons charge exchange on the lunar regolith and are backscattered as negative hydrogen ions. The negative ion fraction is similar to the observed positive ion fraction<sup>1,3</sup>. We estimate a  $\text{H}^-$  surface density of  $0.18^{+0.04}_{-0.03} \text{ cm}^{-3}$ . On the dayside, the lifetime of negative hydrogen ions is short due to photodetachment<sup>10</sup>, confining them to a layer with a scale height of about 10 km. Such surface-bound layers or regions with negative ions should exist at any planetary object with a surface directly exposed to solar wind<sup>11,12</sup>, including low gravity bodies such as asteroids or comets.

The lunar surface is covered by a thick layer of fine grained, porous and weathered material referred to as regolith. As the Moon has almost no atmosphere, the space environment has direct access to the surface. The lunar regolith is continuously modified by impacting micrometeorites and by plasma-surface interaction processes<sup>13,14</sup>. Solar wind ions precipitate onto the lunar surface during most of the Moon's orbit. A majority of them are implanted in the regolith and for example implanted protons are suggested to provide the hydrogen source for the formation of hydroxyl or water molecules present in the topmost regolith layer<sup>15</sup>.

Some of the precipitating ions are directly backscattered to space and can change their charge state in the process<sup>16,17</sup>. At the Moon, up to 1% of the solar wind protons have been seen to backscatter with their original charge state<sup>1–4,18</sup>, while about 5% to 20% of the impinging protons are observed to backscatter as neutral atoms<sup>5,7,19–21</sup>. Additionally, at least 0.14% of the precipitating solar wind alpha particles have been observed to backscatter as neutral helium<sup>6</sup>. Solar wind precipitation also leads to sputtering of surface material<sup>2,6,8,22</sup>. Sputtered particles can be neutral, positively or negatively charged<sup>23,24</sup>. Sputter yields for specific elements or molecules depend on the energy and mass of the precipitating ions as well as on the morphology and composition of the surface<sup>25–28</sup>.

Scattered and sputtered neutral particles with energies below the escape energy contribute to formation of a thin lunar exosphere, together with products from micrometeorite impact vaporisation, photodesorption and gas seeping out from the interior of the Moon<sup>29,30</sup>. Particles with higher energies escape to space and build up the lunar extended corona (Fig. 1).

On the lunar dayside, a non-negligible fraction of the neutral exospheric particles are photoionized<sup>31</sup>, forming an exo-ionosphere<sup>12</sup>. As the surface-bound exo-ionosphere is directly coupled to the interplanetary electric field, its variability is considerable and the ion populations are non-thermal and highly directional<sup>32</sup>. While the main source for ions is photoionization of the exosphere, backscattered and sputtered ions also contribute to the tenuous lunar exo-ionosphere. The lunar exo-ionosphere has been directly detected on the surface<sup>31,33</sup> and been observed from orbit<sup>34</sup>. So far it has mainly been characterised by electron density measurements. Radio occultation observations yielded very high electron densities, later deemed unlikely (see review by Imamura et al.<sup>35</sup>). Shen et al.<sup>36</sup> argue for a typical density of  $1\text{--}10 \text{ cm}^{-3}$  on the dayside and  $<0.1 \text{ cm}^{-3}$  on the nightside, both based on Artemis measurements.

An open question is are there any negative ions in the lunar exo-ionosphere? The lunar surface has long been put forward as a candidate for

<sup>1</sup>Swedish Institute of Space Physics (IRF), Kiruna, Sweden. <sup>2</sup>National Space Science Center (NSSC), Chinese Academy of Sciences (CAS), Beijing, China.

<sup>3</sup>University of Chinese Academy of Sciences, Beijing, China. <sup>4</sup>National Astronomical Observatories, Chinese Academy of Sciences, Beijing, China. <sup>5</sup>These authors contributed equally: Martin Wieser, Aibing Zhang, Romain Canu-Blot, Wengjing Wang, and Stas Barabash. ✉e-mail: [martin.wieser@irf.se](mailto:martin.wieser@irf.se); [zhab@nssc.ac.cn](mailto:zhab@nssc.ac.cn)

**Fig. 1 | Artist's impression of different layers of particle populations formed by solar wind interacting with the lunar surface.**  $H^-$  and  $O^-$  layers are new and inferred from the newly discovered negative ion populations at the surface. Their density is modulated by local magnetic anomalies on the surface. Design: Anastasia Grigoryeva.

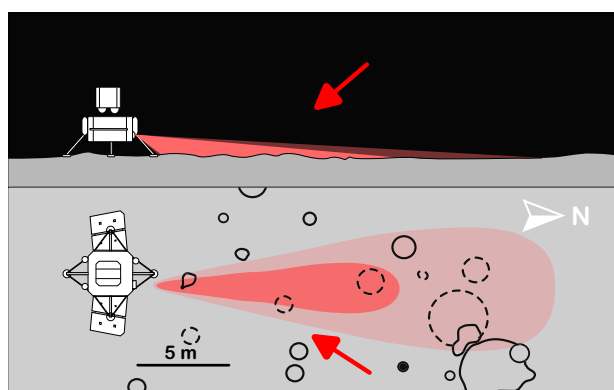
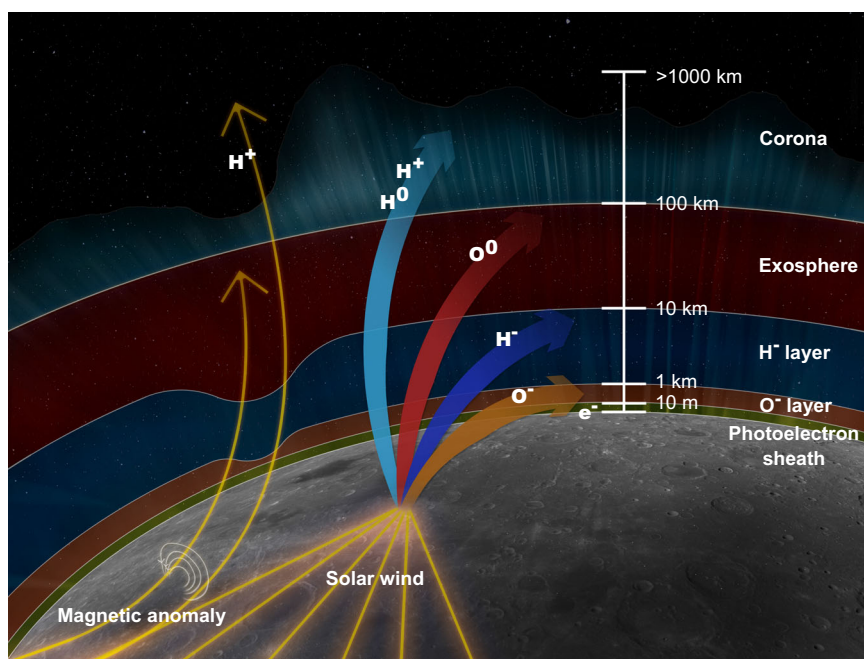


**Fig. 2 | Observation geometry at the lunar surface.** The surface-looking NILS field-of-view is projected onto the lunar surface, approximately to scale (top panel: side view, bottom panel: top view). Local north is towards the right. The light and dark red areas correspond to 20% and 50% sensitivity levels of the footprint, respectively. The red arrow in each view indicates the average direction of solar illumination and is a proxy for the flow direction of the solar wind. Well defined craters are shown as solid lines, degraded craters as dashed lines. The black dot represents a small rock.

the presence of negative ions<sup>11</sup> but no confirmed observation has been done so far. The most obvious reason is the short lifetime of negative ions, making them difficult to observe from orbit. In contrast to positive ions, negative ions will quickly be neutralised by photodetachment. This limits their spatial range considerably. Solar wind protons that charge exchange to  $H^-$  on the lunar surface have an expected lifetime of about 70 ms<sup>10</sup> when illuminated by the Sun. Depending on the negative ion density, negative ions could affect possible plasma wave modes<sup>37</sup>, influence dust charging or influence how plasma enters the lunar wake. Measurements directly on or near the surface are needed to establish the presence of negative ions.

The lander of the Chinese Chang'E-6 sample return mission to the lunar farside<sup>9</sup> carried the Negative Ions at the Lunar Surface (NILS) instrument<sup>38</sup>, an energy and direction resolving negative ion mass analyser, dedicated to establish the presence of negative ions near the lunar surface. NILS is the first-ever dedicated negative ion instrument flown beyond Earth orbit. The NILS instrument was mounted on the Sun-facing side of the Chang'E-6 lander with an unobstructed field-of-view pointing partially to

the surface and partially to the sky. It performed measurements while the lander was operational on the surface.

## Results and discussion

### Observations

On 1 June 2024 at 22:23 UTC Chang'E-6 landed in the predicted landing area<sup>9</sup> in the Apollo crater on the lunar farside at 153.98°W, 41.64°S. The landing site is near the large magnetic anomalies in the South Pole-Aitken basin. NILS operations and data taking started immediately after the completion of post-landing activities and ended when surface operations were finished. For the presented analysis we use 302 minutes of data recorded between 2 June 2024 03:01 UTC and 3 June 2024 03:38 UTC. NILS detected negative ions emitted from a surface area located at a distance from about 1 m to 20 m from the lander (Fig. 2). The sampled surface area was relatively flat and did not contain large craters or boulders.

A distinct  $H^-$  signal was observed (Fig. 3) in the energy range from 50 eV to 400 eV. The differential number flux peaked at about  $4 \times 10^3 \text{ cm}^{-2} \text{ sr}^{-1} \text{ eV}^{-1} \text{ s}^{-1}$ .

The solar zenith angle (ZA) during NILS operations decreased from 52° to 47° with the local solar azimuth angle (SA) changing from 43°E to 28°E. Solar wind parameters for this time period were obtained from the electrostatic analyser instrument (ESA)<sup>39</sup> on the Artemis-P2 spacecraft<sup>40</sup> in lunar orbit. The mean and the standard deviation of the solar wind proton speed and density were  $299 \pm 6 \text{ km/s}$  ( $\approx 466 \text{ eV}$ ) and  $8.1 \pm 2.2 \text{ cm}^{-3}$ , respectively. The solar wind proton speed was rather low during NILS operations. In the years 2000 to 2024, the solar wind proton speed was slower than 300 km/s only for about 3% of the time. The Moon was outside of the Earth's bowshock and the foreshock region, totally embedded in the undisturbed solar wind. However, conditions very close to the lunar surface at the Chang'E-6 landing site could have been slightly different from orbit, because of the strong nearby local magnetic anomalies<sup>41</sup>. The surface potential in or near a magnetic anomaly may be substantially larger than the average value<sup>42</sup>, resulting in a deceleration of incoming protons.

We approximate the energy spectrum of the observed differential number flux for negative hydrogen ions empirically by a log-normal distribution with a mean energy of the backscattered particles of 239 eV with a one sigma width of the distribution of 151 eV. For an average solar wind proton energy of 466 eV during the observation interval, backscattered negative hydrogen ions have experienced an energy loss of on average about

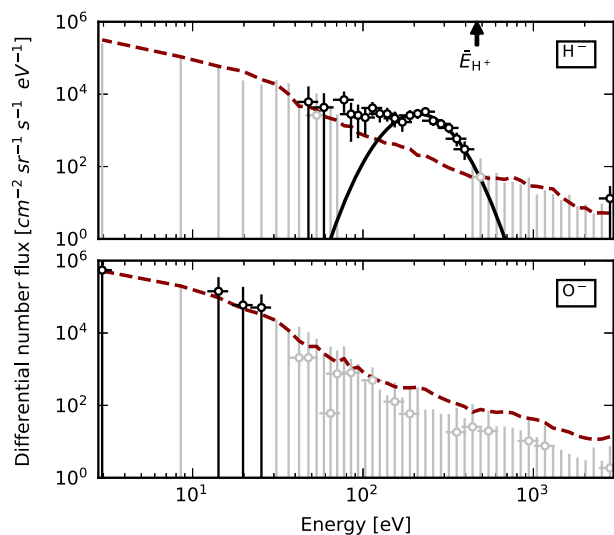


**Fig. 3 | Differential flux of negative ions from the surface.** Top panel: negative hydrogen ion flux, bottom panel: negative oxygen ion flux. The vertical error bars represent 90% confidence intervals and the horizontal error bars represent the energy resolution of the instrument. Black data points are significantly different from zero, grey data points are not. Confidence intervals without a data point indicate that the data point is below the differential flux range shown. The dashed line corresponds to a 90% significance limit below which the differential flux cannot be distinguished from zero. The solid black line is an empirical fit of a log-normal function to the observed  $H^-$  spectrum. The mean solar wind proton energy is indicated by the black arrow.

49%  $\bar{E}_{H^+}$ , assuming the solar wind velocity at the landing site is the same as the one measured by Artemis-P2. The energy spectrum also contains a component between 80 and 150 eV that is above the significance limit and that is not captured by the log-normal distribution used to fit the data. This component likely originates from knock-on sputtered particles<sup>8</sup> from the surface. The low energy tail of the observed spectrum is similar to the low energy hydrogen component observed for energetic neutral atoms<sup>8,43</sup> when convolved with an energy-dependent negative ionisation probability. A similar low energy component has been observed for backscattered protons<sup>4</sup>.

Assuming the observed negative hydrogen ions have the same angular emission distribution from the surface as the one observed for backscattered protons<sup>4</sup>, we can estimate the backscattering yield for negative hydrogen ions,  $Y_{bs,H^-} = J_{bs,H^-} / J_{pre,H^+}$ , with  $J_{bs,H^-}$  [ $cm^{-2} \cdot s^{-1}$ ] the total reflected negative hydrogen ion flux and  $J_{pre}$  [ $cm^{-2} \cdot s^{-1}$ ] the total precipitating solar wind proton flux, respectively. We get  $Y_{bs,H^-} = 2.5^{+1.2}_{-0.8}\%$ . The stated uncertainty is a 90% confidence interval and includes about equal parts counting statistical uncertainties, uncertainties in the instrument calibration<sup>38</sup> and uncertainties in the precipitating solar wind proton flux. The precipitating solar wind flux may be different from the flux observed in orbit by Artemis because of deflection or enhancement effects caused by nearby magnetic anomalies. We estimate the magnitude of such possible variations using the observed variation in the flux of reflected energetic neutral atoms close to a magnetic anomaly<sup>44</sup>. The variation in the reflected energetic neutral atom flux is a proxy for the variation of the solar wind flux precipitating onto the surface.

The observed backscattering yield corresponds to a negative hydrogen density at the surface of  $n_0 = 0.18^{+0.04}_{-0.03} cm^{-3}$  (90% confidence interval). The value is similar to the prediction by Wekhof<sup>11</sup> of  $\approx 0.1 cm^{-3}$ .

Solar wind protons and alpha particles precipitating on the surface also cause sputtering of  $O^-$ . However, the observed  $O^-$  differential flux is close to the significance limit (Fig. 3). Based on that limit, we can only obtain an upper limit of the sputtering yield from incident solar wind protons of  $Y_{sp,O^-} < 19.7\%$ .

**Table 1 | Effect of different assumed  $H^-$  angular scattering functions**

$H^-$ scattering function	$Y_{bs,H^-}$ [%]	$n_0$ [ $cm^{-3}$ ]	$h_0$ [km]
As protons <sup>14</sup>	$2.5^{+1.2}_{-0.8}$	$0.18^{+0.04}_{-0.03}$	9.7
As energetic neutral hydrogen <sup>5</sup>	$2.3^{+1.3}_{-0.7}$	$0.17^{+0.04}_{-0.03}$	8.9
Isotropic	$2.0^{+1.0}_{-0.7}$	$0.14^{+0.03}_{-0.02}$	8.8
Lambert's emission	$2.4^{+1.2}_{-0.8}$	$0.18^{+0.04}_{-0.03}$	10.7

<sup>14</sup>We use data from Lue et al.<sup>4</sup> matching our solar wind speed range (275 km/s to 325 km/s) and solar zenith angle range (45°–60°).

### Backscattered negative hydrogen

The estimated  $H^-$  backscattering yield of  $2.5^{+1.2}_{-0.8}\%$  is comparable to the one for  $H^+$  of 0.01% to 1%<sup>1,3</sup>. The calculation of the backscattering yield depends on the angular distribution of the emitted negative ions. NILS data does not allow to significantly constrain this distribution. Instead, we assumed the angular distribution follows the observed distribution for backscattered protons<sup>4</sup>. We selected this distribution because the charge state of a backscattered particle is established at the end of its interaction with the surface. At that point, the travel direction of the particle has already been established. Choosing a scattering function purely based on observational data has the advantage of including the average influence of the regolith structural properties like regolith grain size and porosity<sup>25,27</sup>. These properties would be difficult to constrain with the limited data set available from NILS. Assuming other angular scattering functions will result in different estimates of the backscattering yield. For example, Vorburger et al.<sup>45</sup> derived an angular emission profile for the backscattering of energetic neutral atoms from Chandrayaan-1<sup>46</sup> data. The backscattering yield for energetic neutral atoms is typically from 5% to 20%<sup>5,7,19–21</sup> and Vorburger et al.<sup>45</sup> find that the emission profile depends on the solar zenith angle. We expect the angular scattering function for charged and neutral particles to be different<sup>4</sup> however. If we nevertheless apply the angular distribution from Vorburger et al.<sup>45</sup> to our observations, we obtain a negative hydrogen ion backscattering yield of about 2.3%—not much different from the value of 2.5% reported above.

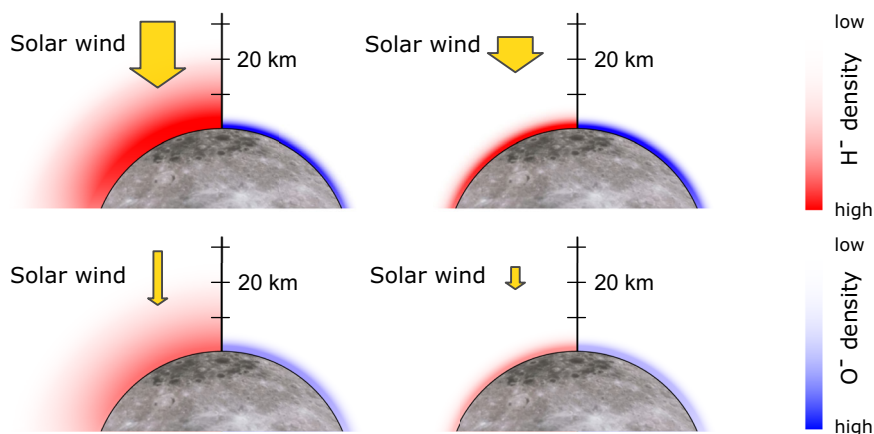
Table 1 shows the effect of different choices in scattering functions on the computed backscattering yield  $Y_{bs,H^-}$ , the negative hydrogen ion surface density  $n_0$ , and the corresponding scale height  $h_0$ . We conclude that the backscattering yield depends on the assumed angular emission profile, but the results are not very sensitive to this choice.

The observed  $H^-$  backscattering yield is larger than the yield observed for  $H^+$ <sup>1–4,18</sup>. A comparably larger yield for  $H^-$  would be compatible with laboratory experiments<sup>16,47</sup> where a negative to positive charge state ratio larger than one for proton backscattering from metals or from oxides was found.

The shape of the observed  $H^-$  differential flux spectrum is very similar to the previously measured backscattered  $H^+$  spectra<sup>3,4</sup>. The average energy loss of 49% obtained for  $H^-$  is slightly different from the 36% given by Lue et al.<sup>3</sup> for  $H^+$ , but it indicates that the backscattered particles experienced only a few collisions with surface atoms. Laboratory measurements of protons scattered from oxides show that the typical energy loss of backscattered hydrogen is independent of the charge state<sup>17,48</sup>. However, the estimate from Lue et al.<sup>3</sup> is an average over a large area of the lunar surface whereas the value reported here for  $H^-$  is a local measurement at the Change'E-6 landing site (Fig. 2).

Reported energy losses are given with respect to the undisturbed solar wind proton energy and the value therefore depends on the local surface potential. A large positive surface potential decelerates the impinging positively charged particles before they interact with the surface. For typical solar wind proton energies, the energy loss is roughly proportional to the incident proton energy, that is, the relative energy loss is constant<sup>17,48</sup>. For a more positive surface potential, the calculated energy loss would be an overestimation. Higher positive surface potentials are expected inside

**Fig. 4 | Negative hydrogen ion density on the lunar dayside.** The scale height of backscattered negative hydrogen ions depends on the solar wind speed (length of yellow arrow) while the scale height for sputtered negative oxygen ions is approximately constant (Moon not to scale). The surface densities of both negative ion species depend on the precipitating solar wind proton flux (width of yellow arrow) and scale with the cosine of the solar zenith angle. This results in an highly dynamic altitude and solar wind parameter dependent negative ion composition which adapts almost instantaneous to changes in solar wind parameters.



magnetic anomalies, where the surface potential can increase by up to 150 V<sup>42</sup>. Assuming the energy losses for both positive and negative backscattered ions are the same, a moderate increase of the local surface potential at the Chang'E-6 landing site by about 50 V could explain the higher energy loss observed in our data. This would be consistent with the proximity of the landing site to the strong nearby local magnetic anomalies of the Aitken basin<sup>41</sup>.

### Sputtered negative oxygen

We do not observe a significant negative oxygen ion flux above the 90% significance limit. Furthermore, below 30 eV, the instrument's field-of-view is constrained to directions quasi-parallel to the lunar surface [38, Fig. 18], making detection of negative ions emitted from the surface a challenge. Fortunately, the trajectories of low-energy ions are considerably affected by the potential structure<sup>49</sup> of the photoelectron sheath. This could make them observable by NILS despite the limitations of the NILS field-of-view at low energies. Models predict rather low sputter yields<sup>50</sup>, but sputtered neutral oxygen has been observed previously<sup>6</sup>, with neutral oxygen flux being 0.2–0.4 times the flux of backscattered neutral hydrogen. With an assumed negative ionisation efficiency of 10%, this gives a sputtering yield for negative oxygen ions of  $Y_{sp,O^-} \approx 0.5\%$ .

The upper limit of 19.7% estimated from NILS data is significantly above this prediction, which explains our non-observation. While the sputtering yield depends on the projectile energy, even a higher solar wind speed is unlikely to have brought the  $O^-$  differential flux above the NILS detection limit<sup>51,52</sup>.

The angular emission function for sputtered  $O^-$  is likely different from the angular scattering function for backscattered  $H^-$ . NILS field-of-view limitations at low energies and the effect of the positive lunar surface potential on the  $O^-$  trajectories make it difficult to estimate what part of the total emitted  $O^-$  flux NILS would observe—even for a known angular emission profile. Thus, only an upper limit for the sputter yield  $Y_{sp,O^-}$  can be given based on NILS data.

Similarly to  $Y_{sp,O^-}$ , an upper limit of the density near the surface can be estimated. We obtain a density for  $O^-$  of  $\lesssim 2.3 \text{ cm}^{-3}$ . The actual value is expected to be at least an order of magnitude lower and comparable to the  $H^-$  density.

### Negative ion layers

The lifetime of negative ions on the lunar dayside is limited and they can travel only short distances before they are neutralised through photo-detachment. The lifetime of  $H^-$  ions is about 70 ms<sup>10</sup>. A backscattered  $H^-$  ion with a typical energy of 239 eV will travel only 15 km on average before it is neutralised. A vertical density profile can be calculated through numerical integration of the angular scattering function. We find a  $H^-$  surface density of  $n_0 \approx 0.18 \text{ cm}^{-3}$  and an equivalent scale height for  $H^-$  of  $h_0 \approx 10 \text{ km}$ , only

weakly dependent on the scattering function choice (Table 1). The scale height is proportional to the average velocity of the emitted negative hydrogen ions which in turn depends on the velocity of the impinging solar wind protons (Fig. 4). Assuming the relative energy loss is the same for a range of typical solar wind proton velocities<sup>17</sup>, the negative hydrogen ion scale height will change proportionally to the solar wind velocity.

Negative oxygen ions have a longer lifetime of 0.6 s before the electron photo-detaches<sup>10</sup>. However, the typical energy of sputtered ions is only a few eV<sup>50</sup>. A sputtered 10 eV  $O^-$  ion travels less than 10 km on the lunar dayside, similar to the distance of a backscattered  $H^-$  ion. Electric fields in the photoelectron sheath will further slow down or deflect sputtered negative particles, considerably reducing their range.

The energy spectrum of sputtered particles is only weakly dependent on the solar wind proton velocity. In contrast to backscattered negative hydrogen ions, the scale height of sputtered negative (oxygen) ions is expected to be rather independent of the solar wind proton velocity (Fig. 4). In addition, low-energy sputtered negative ions are affected by the attractive positive surface potential, which limits their vertical reach. A layer with a negative plasma potential a few tens of metres above the surface<sup>53,54</sup> can further confine sputtered negative ions. Such a layer can form as part of the photoelectron sheath on the dayside close to an altitude where the photoelectron density is approximately equal to the solar wind proton density<sup>49</sup>. This will additionally confine sputtered  $O^-$  to close to the surface.

All negative ions created by precipitating solar wind are thus confined to the surface, forming a surface-bound negative ion layer (Fig. 1). We note that this negative ion layer is expected to show a strongly altitude-dependent composition.

On the lunar nightside, in the absence of solar photons, the lifetime of negative ions is much longer. A negative ion exo-ionosphere will therefore have a substantially larger scale height<sup>11</sup> on the nightside. The challenge is to transport the negative ions to the nightside or to directly generate them there. Negative ions produced close to the optical terminator with high enough energies may escape to the nightside. Despite the rather low near-surface density of negative ions, their contribution to the very tenuous nightside plasma with near-surface densities of positive ions below  $0.02 \text{ cm}^{-3}$ <sup>36</sup> could be significant, at least close to the terminator. Additional negative ions may be produced directly on the nightside by precipitating plasma<sup>55–57</sup>. Micrometeorite impact vaporisation could also be a significant source of low-energy negative ions on the nightside, while it is expected to be a small contribution on the dayside<sup>30,57</sup>. Should the fraction of negative ions be large enough, they can affect the possible wave modes near the lunar surface<sup>37</sup>. Negative ions could affect dust charging. Charged dust is likely to influence plasma instabilities<sup>58,59</sup>.

Negative ion layers or regions (Fig. 1) are expected to be present at all bodies where the surface is exposed to precipitating plasma. This includes Mercury, asteroids, comets and the Martian moons Phobos and Deimos,

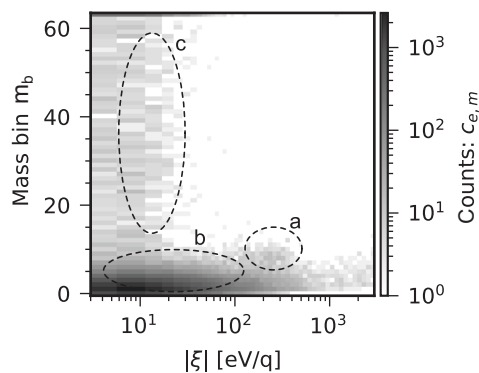


**Fig. 5 | Direction- and time-integrated count matrix  $\mathcal{C}$ .** The count matrix data are plotted against absolute energy-per-charge and mass bin number. Different features are identified: **a** a weak  $\text{H}^-$  signal for energies between 100 eV/q and 400 eV/q; **b** a strong  $\text{e}^-$  peak spanning all energies; and **c** a uniform signal for energies below 30 eV/q attributed to either or both  $\text{O}^-$  and accidental coincidences.

which are exposed to the solar wind, but also, for example, the Galilean moons<sup>12,34,60</sup>, whose surfaces are exposed to the co-rotating Jovian plasma. Farther out in the solar system, the lifetime of negative ions is longer as photo-detachment is less likely. Ignoring other destruction mechanisms, the mean travel distance of negative ions in such environments increases, resulting in more extended negative ion layers. Closer to the Sun, for example at Mercury, the higher photon flux reduces the lifetime of negative ions, resulting in negative ion layers with a smaller scale height.

### Applications

The short spatial range of negative ions creates opportunities for new applications. One example is the possibility to determine surface potential differences at short range. Positively and negatively charged backscattered hydrogen will have energy spectra shifted in opposite directions when observed from a location with a different surface potential. The energy shift is proportional to the surface potential difference between the backscattering location and the observer. This method is similar to the one used by Futaana et al.<sup>42</sup> to obtain surface potential differences by characterising the energy spectrum of backscattered energetic neutral hydrogen.

More sensitive instrumentation should be able to detect sputtered ions, both produced by precipitating solar wind and micrometeorite impacts. Sputtered ions will be useful for surface analysis using secondary ion mass spectrometry (SIMS) [for example<sup>61</sup>]. Using sputtered ions of both charge polarities has the advantage to improved species coverage and sensitivity. For example, strongly electronegative elements like Cl or F are expected to have higher sputtering yields for negative than positive ions. Similarly, negative molecular ions like  $\text{SiO}_2^-$  or  $\text{FeO}_2^-$  facilitate the separation of non-silicate minerals<sup>24</sup>.

### Outlook

The discovery of negative ions close to solar wind exposed surfaces is important not only at the Moon, but concerns all airless bodies in any solar system. The effect of the negative ions on the dynamics of the plasma-surface interaction is a topic of further studies. New missions with dedicated instrumentation for the detection of negative ions will allow to investigate negative ion layers at other planetary bodies. For example the European Space Agency’s JUpiter ICy moons Explorer (JUICE) mission<sup>62</sup> to Jupiter and its moons carries instrumentation able to detect mass resolved negative ions<sup>63</sup>.

## Methods

### Instrumentation

The NILS instrument<sup>38</sup> is a surface interaction-based time-of-flight mass spectrometer for negatively charged particles. It is a further development of the Advanced Small Analyzer for Neutrals instrument flown on Chang’E-4<sup>64</sup>. An adjustable magnetic field across the entrance aperture allows to selectively

suppress the more abundant electrons when measuring negative ions. NILS has a single angular pixel that can be steered in elevation direction to cover a vertically oriented field-of-view of  $\pm 60^\circ$  from the horizon. An electrostatic analyser provides energy coverage from 3 eV per negative charge to 3000 eV per negative charge with 14% energy resolution. The entire energy and angular space is sampled by 16 different viewing directions and 48 energy steps. The geometric factor without efficiencies depends on viewing direction and is between  $0.9 \times 10^{-4} \text{ cm}^2 \text{ sr eV/eV}$  and  $2.4 \times 10^{-4} \text{ cm}^2 \text{ sr eV/eV}$ . Particle velocities are determined in a surface interaction based time-of-flight cell<sup>65</sup>. The measured flight times are converted on-board to an energy independent mass number. For each energy-direction step, the calculated mass numbers are accumulated for 31.25 ms into a mass spectrum histogram. The resulting raw data product is a 3-dimensional energy-direction-mass matrix generated approximately every 100 s. The generation rate is limited by the data transmission from the instrument to the spacecraft.

### Mass separation

This section describes the method used to compute the energy spectra shown in Fig. 3. The fundamental challenge is to separate the contribution of each individual component (or species) that makes up the observed signal. We use knowledge from the calibration of the NILS instrument as well as statistical methods to estimate the flux of each relevant particle species along with its error estimate and statistical significance.

The final data product of the NILS instrument is a time series of 3-dimensional energy-direction-mass count matrices, noted as  $\mathcal{C} = (c_{e,d,m,t})$  with  $c_{e,d,m,t} \in \mathbb{N}_0^{E \times D \times M \times T}$ . The matrix consists of  $E = 48$  energy bins  $e$ ,  $D = 16$  direction bins  $d$ ,  $M = 64$  mass bins  $m$ , and  $T$  measurement sequences  $t$ . For technical reasons, we do not use the highest mass bin from the count matrix  $\mathcal{C}$  as this bin is specially treated during data acquisition [ref. 38, Sect. 4.6]. This reduces the number of mass bins used in our analysis to  $M - 1 = 63$ .

All surface-looking directions pointing to more than  $5^\circ$  below the horizon (Fig. 2) are summed together. Additionally, all measurement sequences are summed together to finally yield the direction- and time-integrated count matrix  $\mathcal{C} = (c_{e,m})$  with  $c_{e,m} \in \mathbb{N}_0^{E \times M}$ . This matrix is available from the Swedish National Data Service<sup>66</sup> and plotted in Fig. 5.

After visual inspection of the resulting count matrix and prior knowledge of the dominant negatively charged species at the lunar surface, we concluded that a total of  $K = 4$  different species contributed to the observed count matrix: electrons, negative hydrogen ions, negative oxygen ions and accidental background counts. While the first three species are actual particles entering the instrument, the fourth species models accidental coincidence events produced when two independent particles create a start and stop event close in time to each other. This accidental contribution is particularly visible at low energies.

The contribution of each of the four species  $k$  to the the count matrix  $\mathcal{C}$  is described by the signal strength matrix  $\theta$ . We define  $\theta = (\theta_{k,e})$  with  $\theta_{k,e} \in \mathbb{R}_0^+$ , defining the contribution of each species  $k$  at each energy bin  $e$ . The time-of-flight responses to electrons, hydrogen, and oxygen ions are empirically estimated in [ref. 38, Sect. 4.6]. We define the time-of-flight response at a mass bin  $m$  to a particle of species  $k$  at an energy bin  $e$  as the function  $f_k(e, m)$ . We neglect uncertainty in these responses and treat them as deterministic quantities. We treat accidental time-of-flight background counts like an own species for which the time-of-flight distribution is assumed to be uniform:  $\mathcal{U}_{[0,1.6\mu\text{s}]}$ , with 1.6  $\mu\text{s}$  the maximum allowed flight time before the system re-initialises.

Each element of  $\mathcal{C}$  is described by a sum of  $K$  independent Poisson distributions such that  $c_{e,m} \sim \text{Poisson}[\lambda_{e,m}(\theta)]$  with

$$\lambda_{e,m}(\theta) \equiv \sum_{k=1}^K \theta_{k,e} f_k(e, m). \quad (1)$$

We use the maximum likelihood method [for example<sup>67</sup>] to find the best estimate of the signal strength matrix  $\theta$  given the observation  $\mathcal{C}$ . In a

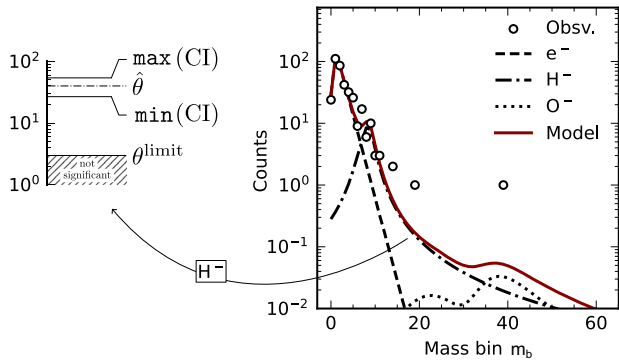


**Fig. 6 | Mass spectrum decomposition example.** Data for energy bin  $e = 25$  is shown. The signal is decomposed into electrons, negative hydrogen ions, negative oxygen ions, and accidental coincidences. The maximum likelihood estimate for negative hydrogen ions, defined in Eq. (3), gives an estimated total number of counts of  $\hat{\theta}_{H^-} \approx 40$ . For  $H^-$ , the significance limit computed from Eq. (8) is about 3 and the 90% confidence limits are  $\min(CI_{H^-}) \approx 28$  and  $\max(CI_{H^-}) \approx 54$ . Accidental coincidences are not shown in the figure as their estimate is below the  $10^{-2}$  count level. The fitted model agrees well over the whole range of mass bins  $m_b$  (note that bins numbers without a data point shown contain zero values that can not be represented in the logarithmic scale).

specific energy bin  $e$ , we define the log-likelihood of the observation as:

$$l_e(\theta; C) \equiv \sum_{m=1}^{M-1} C_{e,m} \ln(\lambda_{e,m}(\theta)) - \lambda_{e,m}(\theta) - \ln(C_{e,m}!). \quad (2)$$

Maximising  $l_e$  at all energies allows us to construct the maximum likelihood estimate  $\hat{\theta}$  as:

$$\hat{\theta} \equiv [\arg \max_{\theta} l_e(\theta; C), \forall e \in \{1, \dots, E\}]. \quad (3)$$

The estimate of the parameter matrix  $\hat{\theta}$  is given in terms of average counts. After converting it to differential number flux, following [ref. 38, Eq. 77], we obtain the black open circles shown in Fig. 3. We performed a visual inspection to assess the goodness-of-fit of the time-of-flight response model to the data. The results did not show noticeable bias or systematic under- or overestimation of the data. An illustration of the method for a single energy bin  $e$  is shown in Fig. 6.

### Significance limit

The significance limit is the flux limit below which a flux is not significantly different from zero. The significance limit (dashed-line in Fig. 3) calculation is based on the profile likelihood ratio<sup>68</sup>, defined in energy bin  $e$  for particle species  $k$ , as

$$\Lambda_e(\theta_{k,e}; C) \equiv 2 \left[ l_e(\hat{\theta}; C) - \max_{\theta_{k,e}=\theta_{k,e}} l_e(\theta; C) \right]. \quad (4)$$

The significance is calculated as the probability to reject the non-existence of a particle species  $k$ , defined by the null hypothesis  $H_0: \theta_k = 0$ , against the alternative  $H_a: \theta_k > 0$ . The null hypothesis is rejected if  $\Lambda_e(\theta_{k,e} = 0; C) > \Lambda_{\text{crit}}$ , with  $\Lambda_{\text{crit}}$  defined by

$$\mathbb{P}[\Lambda_e(\theta_{k,e} = 0; C) \geq \Lambda_{\text{crit}} | H_0] = 1 - \alpha, \quad (5)$$

with  $\alpha = 1 - \text{confidence level}$ . The asymptotic distribution of  $\Lambda_e(\theta_{k,e} = 0; C)$ , under some regulatory conditions<sup>69</sup> and the null hypothesis  $H_0$ , is found analytically [68, Eq. 48] from Wilks' theorem<sup>70</sup> as:

$$\Lambda_e(\theta_k, e = 0; C | H_0) \sim 1/2\delta(0) + 1/2\chi_{\text{dof}}^2, \quad (6)$$

with  $\delta(0)$  the Dirac delta function centred at 0 and dof the degrees of freedom equals to the difference in dimensionality between the maximisation in the nominator and denominator of Eq. (4). Here, dof = 1. From this result, we give a closed form for the critical value  $\Lambda_{\text{crit}}$  as derived in [ref. 68, Eq. 50]:

$$\Phi(\Lambda_{\text{crit}}) = 1 - \alpha, \quad (7)$$

with  $\Phi$  the cumulative distribution function of a unit normal distribution. This gives, for a confidence level of 90%,  $\Lambda_{\text{crit}} \approx 1.64$ .

The significance limit, denoted as  $\theta_{k,e}^{\text{limit}}$ , for a particle species  $k$  in the energy bin  $e$  is calculated as the signal strength for which the expectation value of the test statistics  $\Lambda$  is equal to the critical value above which we reject  $H_0$ :

$$\begin{aligned} \mathbb{E}[\Lambda_e(\theta_{k,e} = 0; C)] &= \Lambda_{\text{crit}}, \\ \text{with } C_{e,m} &\sim \text{Poisson}[\lambda_{e,m}(\hat{\theta} | \theta_{k,e} = \theta_{k,e}^{\text{limit}})], \forall m \in \{1, \dots, M\}. \end{aligned} \quad (8)$$

We used a Monte-Carlo approach to solve Eq. (8) for  $\theta_{k,e}^{\text{limit}}$ , for all particle species  $k$  at all energies  $e$ .

In our example in Fig. 6, the significance limit estimated from Eq. (8) as  $\theta_{H^-}^{\text{limit}} \approx 3$ , confirms that any contribution from  $H^-$  exceeding on average 3 counts is statistically significant.

### Confidence intervals

The confidence region  $CI^\alpha$  at a confidence level of  $(1 - \alpha)$  for each particle species is calculated from the profile likelihood ratio defined in Eq. (4). The confidence region is defined as the set of all signal strength for which the test statistics  $\Lambda$  is small enough as to not being able to reject the null hypothesis  $H_0: \theta_{k,e} = \hat{\theta}_{k,e}$ , with  $\hat{\theta}$  defined in Eq. (3):

$$CI_{k,e}^\alpha(C) \equiv \{\theta_{k,e} | \Lambda_e(\theta_{k,e}; C) \leq \chi_{\text{dof}, 1-\alpha}^2\}, \quad (9)$$

with  $\chi_{\text{dof}, 1-\alpha}^2$  the  $(1 - \alpha)$ th quantile of the  $\chi^2$  distribution with dof = 1 degree of freedom. For a confidence level of 90%, the level of significance is  $\alpha = 10\%$ . The vertical error bars in Fig. 3 bound the minimum and maximum of the confidence region defined in Eq. (9) for each particle species in each energy bin.

In our example in Fig. 6, the confidence interval, derived from Eq. (9) indicates that the true total number of counts from  $H^-$  lies within 90% confidence between  $\min(CI_{H^-}) \approx 28$  and  $\max(CI_{H^-}) \approx 54$ .

For subsequent propagation of error to the differential number flux, the statistical distribution of  $\theta_{k,e}$  for a particle species  $k$  in an energy bin  $e$ , is approximated to the Gamma distribution, such that:

$$\hat{\theta}_{k,e} \sim \text{Gamma}(\alpha, \beta), \text{ with } \begin{cases} F[\min(CI^\alpha); \alpha, \beta] \approx \alpha/2 \\ F[\max(CI^\alpha); \alpha, \beta] \approx (1 - \alpha)/2 \end{cases}, \quad (10)$$

with  $F$  the cumulative distribution function of the Gamma distribution.

### Backscattered negative hydrogen spectrum

The energy spectrum of the average observed differential flux  $j_{\text{obs}, H^-}$  of negative hydrogen ions is fitted by a log-normal distribution

$$j_{\text{fit}, H^-}(E; \bar{j}_{\text{fit}, H^-}, k, \sigma) \equiv \frac{\bar{j}_{\text{fit}, H^-}}{E\sigma\sqrt{2\pi}} \cdot \exp\left(-\frac{(\ln E - \mu)^2}{2\sigma^2}\right), \quad (11)$$

$$\text{with } \mu = \ln(k\bar{E}_{H^+}) - \frac{s^2}{2}, \quad s = \sqrt{\ln(\sigma^2) + 1 - 2\ln(k\bar{E}_{H^+})},$$

where  $E$  is the kinetic energy in eV,  $\bar{j}_{\text{fit}, H^-} \approx 2.7_{-0.8}^{+0.9} \times 10^5 \text{ cm}^{-2} \text{ sr}^{-1} \text{ s}^{-1}$  the energy-integrated differential flux for energies where the flux is above the significance limit,  $\bar{E}_{H^+} \approx 466 \text{ eV}$  the mean upstream solar wind proton

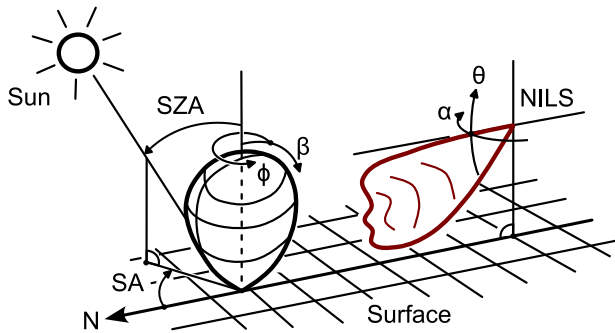


**Fig. 7 | Illustration of angle definitions.** The angular scattering function using spherical coordinates  $(\beta, \phi)$  is shown on the left and the NILS angular response function using instrument spherical coordinates  $(\theta, \alpha)$  on the right. The sun direction is indicated by the solar azimuth angle (SA) and the solar zenith angle (SZA). N points to the local north.

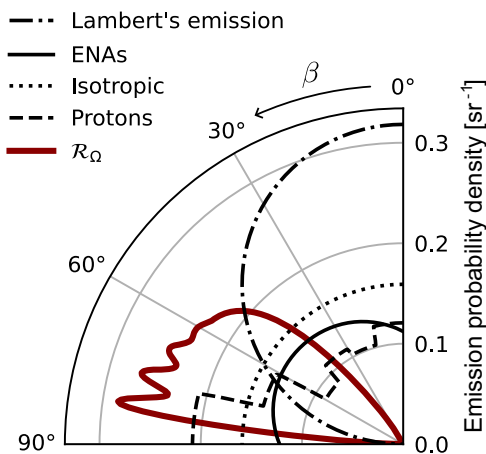


**Fig. 8 | Comparison of scattering functions.** One dimensional slices of the scattering functions for the average NILS solar zenith and azimuth angles, in the direction  $\phi = 215^\circ$  where NILS is the most sensitive are shown. The radial scale of the NILS angular response function  $\mathcal{R}_\Omega$  indicates how sensitive the instrument is in different directions (in arbitrary units).

energy,  $k\bar{E}_{H^+} \approx 239$  eV the mean energy of backscattered particles with  $k = 0.51$ , and  $\sigma = 151$  eV the standard deviation of the energy distribution.

### Angular scattering function and instrument response

This section describes the projection of the NILS angular response function [ref. 38, Sect. 4.4] onto the scattering function to calculate the average observed scattering probability. This probability is required to derive the surface density and scattering yield estimates.

Figure 7 illustrates the definition of the different angles used in the calculation. The lander's attitude is approximated to be levelled perfectly horizontally, with NILS facing north. For a given solar azimuth angle  $SA \in [0, 2\pi)$ , the transformation from the instrument spherical coordinates  $(\theta, \alpha)$  to the scattering function coordinates  $(\beta, \phi)$  is given by the function  $f: [0, 2\pi) \times [-\pi/2, \pi/2) \rightarrow [0, \pi/2) \times [0, 2\pi)$  such, that for  $\theta \in [3\pi/2, 2\pi)$ , the components of  $f = (f_1, f_2)$  are given by:

$$\beta = f_1(\theta) = \arctan\left(\frac{-\cos\theta}{\sin\theta}\right), \quad (12)$$

$$\phi = f_2(\theta, \alpha; SA) = \left[\pi + SA - \arctan\left(\frac{-\sin\alpha}{\cos\alpha \cos\theta}\right)\right] \bmod 2\pi, \quad (13)$$

with  $\phi$  the scattering azimuth angle equalling zero toward the Sun, and  $\beta$  the scattering polar angle equalling zero for the zenith-pointing direction. For

$\theta \in [0, 3\pi/2)$ , the transformation  $f$  is undefined. The inverse of the transformation  $f$ , noted as  $f^{-1}$ , has the components

$$\theta = f_1^{-1}(\beta) = \arcsin\left(\frac{\tan\beta}{\sqrt{\frac{2}{\cos(2\beta)+1}}}\right) - \pi/2, \quad (14)$$

$$\alpha = f_2^{-1}(\beta, \phi; SA) = -\arctan\left[\frac{\tan\beta \tan(SA - \phi)}{\sqrt{\tan^2\beta + 1}}\right]. \quad (15)$$

The Jacobian determinant of the transformation  $f^{-1}$  is

$$\det(\mathbf{J}_{f^{-1}}(\beta, \phi; SA)) = \left[\tan\beta \cos\beta \left[\frac{\cos^2(SA - \phi)}{\tan^2\beta} + 1\right]\right]^{-1}. \quad (16)$$

We define as  $\Gamma$  [ $\text{sr}^{-1}$ ] the average observed emission probability density, that is, the average probability density that a particle impacting the lunar surface is scattered and detected by the NILS instrument:

$$\Gamma(\text{SZA}, SA) \equiv \int_0^{2\pi} \int_0^{\pi/2} \mathcal{R}_\Omega(f^{-1}(\beta, \phi; SA)) \mathcal{F}(\beta, \phi; \text{SZA}) \cdot \det(\mathbf{J}_{f^{-1}}(\beta, \phi; SA)) d\beta d\phi, \quad (17)$$

with  $\mathcal{F}$  [ $\text{sr}^{-1}$ ] the scattering function, normalised such that  $\iint \mathcal{F}(\beta, \phi) \sin\beta d\beta d\phi = 1$  and  $\mathcal{R}_\Omega$  [ $\text{sr}^{-1}$ ] the angular response of NILS as defined in [ref. 38, Eq. 15].

The scattering functions for protons and energetic neutral hydrogen are defined as in Lue et al.<sup>4</sup> and Vorburger et al.<sup>45</sup>, respectively. We choose to work with two additional arbitrary scattering functions based on isotropic and Lambert's emission profiles, defined as

$$\mathcal{F}_{\text{isotropic}}(\beta, \phi) = \frac{1}{2\pi}, \quad (18)$$

$$\mathcal{F}_{\text{Lambert}}(\beta, \phi) = \frac{\cos\beta}{\pi}. \quad (19)$$

Figure 8 shows a comparison of the different scattering functions with the NILS angular response function  $\mathcal{R}_\Omega$ .

### Backscattering yield for negative hydrogen

We define the solar wind backscattering yield  $Y_{\text{bs}, H^-}$  as the ratio of the backscattered negative hydrogen flux  $J_{\text{bs}, H^-}$  [ $\text{cm}^{-2} \text{s}^{-1}$ ] and the precipitating flux  $J_{\text{pre}, H^+}$  [ $\text{cm}^{-2} \text{s}^{-1}$ ]. We approximate the precipitating flux by the undisturbed upstream solar wind flux  $J_{\text{sw}}$  [ $\text{cm}^{-2} \text{s}^{-1}$ ] impinging from a given solar zenith angle (SZA) to the surface. NILS observes a negative hydrogen differential flux  $j_{\text{obs}, H^-}$  [ $\text{cm}^{-2} \text{sr}^{-1} \text{eV}^{-1} \text{s}^{-1}$ ] emitted from a scattering function which average observed scattering probability is noted as  $I$ . The energy spectrum is assumed to be independent of the emission angles  $(\beta, \phi)$ . This finally gives a description for the yield given by

$$J_{\text{pre}, H^+} = J_{\text{sw}} \cos(\text{SZA}) \quad (20)$$

$$J_{\text{bs}, H^-} = \Gamma^{-1} \int_0^\infty j_{\text{fit}, H^-} dE \quad (21)$$

$$Y_{\text{bs}, H^-} = J_{\text{bs}, H^-} / J_{\text{pre}, H^+} \quad (22)$$

The uncertainty of the backscattering yield is calculated based on the uncertainty in  $j_{\text{obs}, H^-}$ , the uncertainty in  $J_{\text{sw}}$  and the variation of the solar zenith and azimuth angle over the NILS mission. Table 1 shows shows best estimates of the backscattering yield along with its 90% confidence interval.

### Upper limit for sputtered negative oxygen

The flux of negative oxygen ions is below the 90% significance limit and only an upper limit for the sputtering yield for  $Y_{\text{sp},\text{O}^-}$  can be estimated. An additional complication is that the NILS field of view below 100 eV is energy dependent. For low energies is focused around the horizon direction<sup>38</sup>. Low energy trajectories are affected by local electric fields from the photoelectron sheath and a possibly non-zero spacecraft potential. For simplicity, we assume that the angular emission profile follows Lambert's emission profile:

$$Y_{\text{sp},\text{O}^-} = \frac{J_{\text{sp},\text{O}^-}}{J_{\text{pre},\text{H}^+}} \approx \frac{\Gamma^{-1} \int_0^\infty j_{\text{sig},\text{O}^-}(E) dE}{J_{\text{sw}} \cos(\text{SZA})}, \quad (23)$$

with  $\Gamma \approx 8.5 \times 10^{-2} \text{ sr}^{-1}$ , obtained for the average solar zenith and azimuth angles over the NILS mission.

### Surface density estimate

The negative hydrogen ion density at the surface  $n_0$  [ $\text{m}^{-3}$ ] is calculated as

$$n_0 = \Gamma^{-1} \int_0^\infty \sqrt{\frac{m}{2E}} \cdot j_{\text{fit},\text{H}^-}(E) dE, \quad (24)$$

with  $j_{\text{fit},\text{H}^-}(E)$  [ $\text{m}^{-2} \text{ sr}^{-1} \text{ eV}^{-1} \text{ s}^{-1}$ ] the fitted differential number flux for negative hydrogen ions (Fig. 3, note different units),  $E$  the energy in J, and  $m$  the proton mass in kg.

An upper limit of the negative oxygen ion density is estimated by replacing  $j_{\text{fit},\text{H}^-}$  with the significance limit for negative oxygen ions  $j_{\text{sig},\text{O}^-}$  and assuming a Lambert's emission profile.

### Scale height estimate

We obtain an estimate for the scale height of the  $\text{H}^-$  layer by numerically integrating the observed energy spectrum for all emission angles. The mean lifetime on the lunar dayside of  $\text{H}^-$  is  $\tau \approx 70 \text{ ms}$ <sup>10</sup>,  $m$  denotes the proton mass and  $E$  the energy in J. The resulting function  $n(h)$  is fitted by an exponential to obtain the scale height  $h_0$ .

$$n(h) = \Gamma^{-1} \int_0^{2\pi} \int_0^{\frac{\pi}{2}} \int_0^\infty \exp\left(\frac{-h}{\tau E \cos \beta}\right) j_{\text{fit},\text{H}^-}(E) \sqrt{\frac{m}{2E}} \mathcal{F}(\beta, \phi) dE d\beta d\phi$$

$$\approx n_0 \exp\left(-\frac{h}{h_0}\right) \quad (25)$$

### Data availability

The NILS data set<sup>66</sup> used in this article is available at the Swedish National Data Service (SND), <https://researchdata.se/en/catalogue/dataset/2024-442>, <https://doi.org/10.5878/v4sy-3t95>.

### Code availability

Relevant processing code is accompanying the NILS data set<sup>66</sup> available at the Swedish National Data Service.

Received: 26 December 2024; Accepted: 19 May 2025;

Published online: 10 June 2025

### References

- Saito, Y. et al. Solar wind proton reflection at the lunar surface: low energy ion measurement by MAP-PACE onboard SELENE (Kaguya). *Geophys. Res. Lett.* **35**, L24205 (2008).
- Tanaka, T. et al. First in situ observation of the moon-originating ions in the earth's magnetosphere by map-pace on selene (Kaguya). *Geophys. Res. Lett.* **36**, L22106 (2009).
- Lue, C. et al. Chandrayaan-1 observations of backscattered solar wind protons from the lunar regolith: dependence on the solar wind speed. *J. Geophys. Res. Planets* **119**, 968–975 (2014).
- Lue, C., Halekas, J. S., Poppe, A. R. & McFadden, J. P. Artemis observations of solar wind proton scattering off the lunar surface. *J. Geophys. Res. Space Phys.* **123**, 5289–5299 (2018).
- Wieser, M. et al. Extremely high reflection of solar wind protons as neutral hydrogen atoms from regolith in space. *Planet. Space Sci.* **57**, 2132–2134 (2009).
- Vorburger, A. et al. First direct observation of sputtered lunar oxygen. *J. Geophys. Res. Space Phys.* **119**, 709–722 (2014).
- Zhang, A. et al. Emission of energetic neutral atoms measured on the lunar surface by Chang'E-4. *Planet. Space Sci.* **189**, 104970 (2020).
- Wieser, M. et al. Energy spectra of energetic neutral hydrogen backscattered and sputtered from the lunar regolith by the solar wind. *Astron. Astrophys.* **684**, A146 (2024).
- Zeng, X. et al. Landing site of the Chang'e-6 lunar farside sample return mission from the Apollo basin. *Nat. Astron.* **7**, 1188–1197 (2023).
- Desai, R. T., Zhang, Z., Wu, X. & Lue, C. Photodetachment and test-particle simulation constraints on negative ions in solar system plasmas. *Planet. Sci. J.* **2**, 99 (2021).
- Wekhof, A. Negative ions in the ionospheres of planetary bodies without atmospheres. *moon planets* **24**, 45–52 (1981).
- Farrell, W. et al. Regarding the possible generation of a lunar nightside exo-ionosphere. *Icarus* **216**, 169–172 (2011).
- Keller, L. P. & McKay, D. S. The nature and origin of rims on lunar soil grains. *Geochim. Cosmochim. Acta* **61**, 2331–2341 (1997).
- Farrell, W. M. et al. The dust, atmosphere, and plasma at the moon. *Rev. Mineral. Geochem.* **89**, 563–609 (2023).
- Zhou, C. et al. Chang'e-5 samples reveal high water content in lunar minerals. *Nat. Commun.* **13**, 5336 (2022).
- Verbeek, H., Eckstein, W. & Datz, S. Positive and negative hydrogen ions backscattered from au, ta, and tho2 in the energy range up to 15 kev. *J. Appl. Phys.* **47**, 1785–1789 (1976).
- Wieser, M., Wurz, P., Bruning, K. & Heiland, W. Scattering of atoms and molecules off a magnesium oxide surface. *Nucl. Instr. Meth. B* **192**, 370–380 (2002).
- Lue, C. et al. Strong influence of lunar crustal fields on the solar wind flow. *Geophys. Res. Lett.* **38**, L03202 (2011).
- McComas, D. J. et al. Lunar backscatter and neutralization of the solar wind: first observations of neutral atoms from the moon. *Geophys. Res. Lett.* **36**, L12104 (2009).
- Rodríguez, M. D. F. et al. Ibex-lo observations of energetic neutral hydrogen atoms originating from the lunar surface. *Planet. Space Sci.* **60**, 297–303 (2012).
- Saul, L. et al. Solar wind reflection from the lunar surface: The view from far and near. *Planet. Space Sci.* **84**, 1–4 (2013).
- Yokota, S. et al. First direct detection of ions originating from the Moon by MAP-PACE IMA onboard SELENE (KAGUYA). *Geophys. Res. Lett.* **36**, L11201 (2009).
- Taglauer, E. & Heiland, W. (eds.). *Theory of Charge States in Sputtering* (Springer Berlin Heidelberg, 1981).
- Rinnen, S., Stroth, C., Riße, A., Ostertag-Henning, C. & Arlinghaus, H. F. Characterization and identification of minerals in rocks by ToF-SIMS and principal component analysis. *Appl. Surf. Sci.* **349**, 622–628 (2015).
- Szabo, P. S. et al. Energetic neutral atom (ena) emission characteristics at the moon and mercury from 3d regolith simulations of solar wind reflection. *J. Geophys. Res.: Planets* **128**, e2023JE007911 (2023).
- Leblanc, F. et al. On the origins of backscattered solar wind energetic neutral hydrogen from the moon and mercury. *Planet. Space Sci.* **229**, 105660 (2023).

27. Verkercke, S. et al. Effects of airless bodies' regolith structures and of the solar wind's properties on the backscattered energetic neutral atoms flux. *Planet. Sci. J.* **4**, 197 (2023).
28. Killen, R. M. et al. The influence of surface binding energy on sputtering in models of the sodium exosphere of mercury. *Planet. Sci. J.* **3**, 139 (2022).
29. Lucey, P. et al. Understanding the lunar surface and space-moon interactions. *Rev. Mineral. Geochem.* **60**, 83–219 (2006).
30. Wurz, P. et al. The lunar exosphere: the sputtering contribution. *ICARUS* **191**, 486–496 (2007).
31. Lindeman, R., Freeman, J. J. W. & Vondrak, R. R. Ions from the lunar atmosphere. *Lunar Planet. Sci. Conf. Proc.* **4**, 2889 (1973).
32. Stern, S. A. The lunar atmosphere: History, status, current problems, and context. *Rev. Geophys.* **37**, 453–491 (1999).
33. Reasoner, D. L. & Burke, W. J. Characteristics of the lunar photoelectron layer in the geomagnetic tail. *J. Geophys. Res.* (1896–1977) **77**, 6671–6687 (1972).
34. Halekas, J. S. et al. A tenuous lunar ionosphere in the geomagnetic tail. *Geophys. Res. Lett.* **45**, 9450–9459 (2018).
35. Imamura, T. et al. Studying the lunar ionosphere with selene radio science experiment. *Space Sci. Rev.* **154**, 305–316 (2010).
36. Shen, H.-W., Halekas, J. S. & Poppe, A. R. Limits on the density of the lunar ionosphere: Artemis observations. *Astrophys. J.* **958**, 165 (2023).
37. D'Angelo, N., Goeler, S. V. & Ohe, T. Propagation and damping of ion waves in a plasma with negative ions. *Phys. Fluids* **9**, 1605–1606 (1966).
38. Canu-Blot, R. et al. The Negative Ions at the Lunar Surface (NILS) Instrument on the Chang'E-6 Mission. *Space Sci. Rev.* **221**, 38 (2025).
39. McFadden, J. P. et al. The THEMIS ESA Plasma Instrument and In-flight Calibration. *Space Sci. Rev.* **141**, 277–302 (2008).
40. Angelopoulos, V. The artemis mission. *Space Sci. Rev.* **165**, 3–25 (2011).
41. Hood, L. L., Torres, C. B., Oliveira, J. S., Wicczorek, M. A. & Stewart, S. T. A new large-scale map of the lunar crustal magnetic field and its interpretation. *J. Geophys. Res. Planets* **126**, e2020JE006667 (2021).
42. Futaana, Y. et al. Remote energetic neutral atom imaging of electric potential over a lunar magnetic anomaly. *Geophys. Res. Lett.* **40**, 262–266 (2013).
43. Kenmotsu, T., Yamamura, Y., Ono, T. & Kawamura, T. A new formula for energy spectrum of sputtered atoms due to low-energy light ions. *J. Plasma Fusion Res.* **80**, 406–409 (2004).
44. Wieser, M. et al. First observation of a mini-magnetosphere above a lunar magnetic anomaly using energetic neutral atoms. *Geophys. Res. Lett.* **37**, L05103 (2010).
45. Vorburger, A. et al. Energetic neutral atom imaging of the lunar surface. *J. Geophys. Res.: Space Phys.* **118**, 3937–3945 (2013).
46. Barabash, S. et al. Investigation of the solar wind–Moon interaction onboard Chandrayaan-1 mission with the SARA experiment. *Curr. Sci.* **96**, 526–532 (2009).
47. Niehus, H., Heiland, W. & Taglauer, E. Low energy ion scattering at surfaces. *Surf. Sci. Rep.* **17**, 213–303 (1993).
48. Jans, S. et al. Scattering of atoms and molecules on a barium zirconate surface. *Nucl. Instr. Meth. B* **173**, 503–515 (2001).
49. Li, L., Zhang, Y.-T., Zhou, B. & Feng, Y.-Y. Lunar surface potential and electric field. *Res. Astron. Astrophys.* **19**, 077 (2019).
50. Jäggi, N. et al. New compound and hybrid binding energy sputter model for modeling purposes in agreement with experimental data. *Planet. Sci. J.* **4**, 86 (2023).
51. Roth, J., Bohdansky, J. & Ottenberger, W. *Data on Low Energy Light Ion Sputtering. Technical Report IPP 9/26* (Max-Planck-Institut für Plasmaphysik, 1979).
52. Schaible, M. J. et al. Solar wind sputtering rates of small bodies and ion mass spectrometry detection of secondary ions. *J. Geophys. Res. Planets* **122**, 1968–1983 (2017).
53. Guernsey, R. L. & Fu, J. H. M. Potential distribution surrounding a photo-emitting, plate in a dilute plasma. *J. Geophys. Res.* **75**, 3193–3199 (1970).
54. Nitter, T., Havnes, O. & Melandsø, F. Levitation and dynamics of charged dust in the photoelectron sheath above surfaces in space. *J. Geophys. Res.: Space Phys.* **103**, 6605–6620 (1998).
55. Farrell, W. et al. Anticipated electrical environment within permanently shadowed lunar craters. *J. Geophys. Res. Planets* **115** (2010).
56. Nishino, M. N. et al. Solar-wind proton access deep into the near-moon wake. *Geophys. Res. Lett.* **36**, L16103 (2009).
57. Wurz, P. et al. Particles and photons as drivers for particle release from the surfaces of the moon and mercury. *Space Sci. Rev.* **218**, 10 (2022).
58. Vladimirov, S. V., Ostrikov, K., Yu, M. Y. & Morfill, G. E. Ion-acoustic waves in a complex plasma with negative ions. *Phys. Rev. E* **67**, 036406 (2003).
59. Rosenberg, M. & Merlino, R. Ion-acoustic instability in a dusty negative ion plasma. *Planet. Space Sci.* **55**, 1464–1469 (2007).
60. Nordheim, T. A. et al. Detection of negative pickup ions at saturn's moon dione. *Geophys. Res. Lett.* **47**, e2020GL087543 (2020).
61. Lockyer, N. P. et al. Secondary ion mass spectrometry. *Nat. Rev. Methods Prim.* **4**, 32 (2024).
62. Grasset, O. et al. Jupiter icy moons explorer (juice): an esa mission to orbit ganymede and to characterise the jupiter system. *Planet. Space Sci.* **78**, 1–21 (2013).
63. Wittmann, P. *The Jovian Plasma Dynamics and Composition Analyzer (JDC) for ESA's JUICE Mission*. Ph.D. thesis (Swedish Institute of Space Physics, Umeå University, 2022).
64. Wieser, M. et al. The Advanced Small Analyzer for Neutrals (ASAN) on the Chang'E-4 Rover Yutu-2. *Space Sci. Rev.* **216**, 73 (2020).
65. Wieser, M. & Barabash, S. A family for miniature, easily reconfigurable particle sensors for space plasma measurements. *J. Geophys. Res.: Space Phys.* **121**, 11,588–11,604 (2016).
66. Wieser, M., Zhang, A. & the NILS team. Negative ion mass spectrum from observations by the Negative Ion at the Lunar Surface (NILS) instrument onboard of the Chang'E-6 lunar lander (Version 3). Swedish Institute of Space Physics (2025).
67. Le Cam, L. Maximum likelihood: an introduction. *Int. Stat. Rev. / Rev. Int. de Stat.* **58**, 153–171 (1990).
68. Cowan, G., Cranmer, K., Gross, E. & Vitells, O. Asymptotic formulae for likelihood-based tests of new physics. *The Eur. Phys. J. C* **71**, 1554 (2011).
69. Algeri, S., Aalbers, J., Morà, K. D. & Conrad, J. Searching for new phenomena with profile likelihood ratio tests. *Nat. Rev. Phys.* **2**, 245–252 (2020).
70. Wilks, S. S. The large-sample distribution of the likelihood ratio for testing composite hypotheses. *Ann. Math. Stat.* **9**, 60–62 (1938).

## Acknowledgements

For solar wind parameters we acknowledge the use of ARTEMIS-P2 (THEMIS-C) data via NASA/GSFC's Space Physics Data Facility's OMNIWeb (or CDAWeb) service, and OMNI data. The Negative Ions on the Lunar Surface (NILS) instrument was developed by the Swedish Institute of Space Physics (IRF) in Kiruna, Sweden, on behalf of the European Space Agency (ESA). It was supported by the ESA grant No. 3-17483/22/NL/DB. Activities at NSSC were supported by the National Natural Science Foundation of China (NSFC), grant no. 42441807.

## Author contributions

Martin Wieser and Aibing Zhang were leading the project and were involved in all aspects including the manuscript. Romain Canu-Blot calibrated the NILS instrument, analysed the data and wrote the manuscript. Wengjing Wang managed the project for NSSC and the China National Space Administration CNSA. Gabriella Stenberg Wieser wrote the manuscript. Lianghai Xie was involved in initial studies, Stas Barabash formulated the original scientific question, developed the NILS architecture, defined and initiated the project, and coordinated activities. Tianhua Zhong was involved

in data processing and verification, Máté Kerényi and Xiao-Dong Wang managed the NILS project for the Swedish Institute of Space Physics. Yongliao Zou and Chi Wang initiated the project for NSSC, and coordinated activities in China, Charles Lue was involved in initial studies, Weibin Wen was involved in data receiving and preliminary processing.

### Competing interests

The authors declare no competing interests.

### Additional information

**Supplementary information** The online version contains supplementary material available at <https://doi.org/10.1038/s43247-025-02399-7>.

**Correspondence** and requests for materials should be addressed to Martin Wieser or Aibing Zhang.

**Peer review information** *Communications Earth & Environment* thanks the anonymous reviewers for their contribution to the peer review of this work. Primary Handling Editors: Brittany Cymes and Joe Aslin. A peer review file is available.

**Reprints and permissions information** is available at <http://www.nature.com/reprints>

**Publisher's note** Springer Nature remains neutral with regard to jurisdictional claims in published maps and institutional affiliations.

**Open Access** This article is licensed under a Creative Commons Attribution 4.0 International License, which permits use, sharing, adaptation, distribution and reproduction in any medium or format, as long as you give appropriate credit to the original author(s) and the source, provide a link to the Creative Commons licence, and indicate if changes were made. The images or other third party material in this article are included in the article's Creative Commons licence, unless indicated otherwise in a credit line to the material. If material is not included in the article's Creative Commons licence and your intended use is not permitted by statutory regulation or exceeds the permitted use, you will need to obtain permission directly from the copyright holder. To view a copy of this licence, visit <http://creativecommons.org/licenses/by/4.0/>.

© The Author(s) 2025